CEAS Aeronautical Journal
https://doi.org/10.1007/s13272-024-00760-8

ORIGINAL PAPER

Unsteady nonlinear lifting line model for active gust load alleviation of airplanes

Yannic Beyer[1] · Junaid Ullah[2] · Meiko Steen[1] · Peter Hecker[1]

Received: 23 August 2023 / Revised: 7 May 2024 / Accepted: 9 July 2024
© The Author(s) 2024

Abstract
Active gust load alleviation is an important technology for designing future passenger airplanes to be lighter and thus more environmentally friendly. Unsteady Reynolds-averaged Navier–Stokes (URANS) simulations are typically used to accurately calculate gust loads, but because of their high computational cost, they can only be performed at a few selected operating points. In simpler potential theory models, stall is neglected, resulting in loss of accuracy. In this paper, a low-order unsteady aerodynamics wing model is presented, which is able to represent well compressible flow with stall. Furthermore, the model offers the possibility to modularly incorporate actuators, which allows the design and evaluation of active load alleviation systems. The model is based on a conventional unsteady 2D airfoil model including a dynamic stall model. The dynamic stall model requires viscous steady coefficients, e.g. from 2D steady RANS computations. This 2D airfoil model is coupled with a 3D steady-state lifting line model. The model is applied to the LEISA research airplane and extensively validated with URANS results. It performs well in calculating gust loads with and without simultaneous flap deflections, and provides significantly more accurate results in the case of stall than when stall is neglected.

Keywords Lifting line · Unsteady aerodynamics · Dynamic stall · Gust load alleviation

1 Introduction

For the certification of commercial aircraft, it must be demonstrated, among other load cases, that the structure can withstand strong gusts. The requirements are described in FAR25 and CS25 [1, 2]. Several methods are available for calculating gust loads [3]. However, accurate calculation of gust loads is difficult because complex aerodynamic processes must be considered. Wu et al. [4] provide an overview about gust load codes. Dussart et al. [3] makes a rough ranking of aerodynamic models according to complexity and fidelity. Highfidelity methods such as unsteady Reynolds-averaged Navier–Stokes (URANS) simulations can be used to calculate the aerodynamics very accurately [5]. But due to the enormous computational effort, this method is only available for a limited number of selected operating points. Midfidelity methods such as doublet-lattice method (DLM) or unsteady vortex-lattice method (UVLM) are used by default on a large scale to calculate gust loads [5]. However, these methods are based on the assumption of incompressible, frictionless flow as well as flat bodies. While the influence of compressibility can be easily and well corrected [6], the nonlinear behavior of stall is difficult to correct. Without correction for stall, gust loads may be calculated too large, i.e., conservatively [7, 8]. DeLaurier [9] introduced the modified strip theory (MST), a lowfidelity method based on the principle of indicial functions, which is often used for aeroelastic flight dynamics models [3, 10–12]. However, this method, unlike DLM and UVLM, does not consider spanwise flow interactions. Ritter et al. [13] found significant errors in strip theory when comparing strip theory and various UVLM programs for gust loads. MST, as described

✉ Yannic Beyer
y.beyer@tu-bs.de

Junaid Ullah
ullah@iag.uni-stuttgart.de

Meiko Steen
m.steen@tu-bs.de

Peter Hecker
p.hecker@tu-bs.de

[1] Institute of Flight Guidance, Technische Universität Braunschweig, Hermann-Blenk-Str. 27, 38108 Brunswick, Germany

[2] Institute of Aerodynamics and Gas Dynamics, University of Stuttgart, Pfaffenwaldring 21, 70569 Stuttgart, Germany

Published online: 05 August 2024

by Andrews [10], was compared to (steady) RANS simulation results in [14], and high accuracy is found. However, the comparison is limited to steady-state operating points. MST was extended by Kim et al. [15] to take dynamic stall into account, which is quite easy with this method since 2D airfoil dynamic stall can be used.

For 2D airfoil flows, semi-empirical models of low order are long established for dynamic stall due to their simplicity and satisfactory accuracy [16, 17]. These models are based on the concept of indicial functions by using linear differential equations which approximate the Wagner function [18]. This linear model is extended by a delayed flow separation point ahead of the trailing edge and an optional dynamic leadingedge vortex, both requiring nonlinear steady-state lift coefficients with stall. These 2D steady-state lift coefficients can be obtained from RANS simulations or experimentally with comparatively little effort.

There are also numerous publications on corrections with viscous 2D airfoil data for steady-state 3D wing flows [19–24]. Van Dam [20] coupled a finitestep method of Weissinger [25], which is a lifting line method, with 2D viscous section data. The viscous correction is applied iteratively by changing the section angle of attack. Gallay et al. [21] added a modification which results in better convergence and unique solution in post-stall scenarios. However, the previously mentioned publications on 3D wing flows do not provide models for unsteady flows.

Parenteau et al. [26] propose two unsteady models for 3D wings. The first model, however, does not include dynamic stall, the second model requires unsteady 2D airfoil solutions and covers only periodic dynamic stall. Sugar-Gabor [27] presents an unsteady lifting line model that features the geometrically discretized circulation used in UVLM in the wake. The model is coupled with viscous 2D airfoil data. While the steady-state lift and drag coefficients look satisfactory up to the onset of stall, we doubt good results for dynamic stall since no model is included for the flow separation point as is typical for 2D models (see above). Dias [28] has coupled a lifting line method with a dynamic stall model, which shows good agreement with experimental data. However, this model is limited to unswept wings and is only superficially described.

Previous work about gust load alleviation [7, 8, 29] has shown that dynamic stall may influence the peak gust loads of airplanes using costly URANS simulations. In that work, 2D and 3D calculations were performed while the aircraft is not free to pitch or plunge. In addition, dynamic trailing-edge flap deflections are simulated with and without simultaneous gust interaction. With this paper, we aim to provide the following contributions. The aim of this work is to efficiently and accurately reproduce these results. Therefore, we present a novel efficient continuous-time unsteady aerodynamics wing model which accounts for stall. An overview of the model was already shown in [30]. The model is a coupling of lifting line (LL) method with the concept of indicial functions (IF) including a nonlinear (NL) dynamic stall model. In the further course the model is called *nonlinear indicial functions lifting line* (NL-IF-LL) model. The model includes a modular implementation of spanwise distributed actuators. Moreover, the model is implemented in the publicly available *Library of Aircraft Dynamics and Control*.[1] For validation, the presented model is compared with URANS simulation results for gust simulations and dynamic trailing-edge flap deflections.

When calculating gust loads of airplanes, the flexible movements of the airplane must of course be taken into account. Nevertheless, since this work is only concerned with the aerodynamics model and its validation, the use of a rigid and unaccelerated aircraft is reasonable to avoid additional, unnecessary complexity. A coupling of the NL-IF-LL model with flexible equations of motion is of course possible, but not the subject of this work. Incidentally, the conditions of a rigid and unaccelerated airplane are approximately satisfied in gust interactions when precise flap deflections are simultaneously executed to compensate for the gust loads.

The outline of the paper is as follows. Section 2 presents the NL-IF-LL model in detail. In Sect. 3, results of the NL-IF-LL model are compared with RANS and URANS models for different scenarios. Finally, Sect. 4 draws conclusions and summarizes the limitations.

2 Unsteady nonlinear lifting line model

In this section, the NL-IF-LL model is described. Figure 1 shows an overview of the NL-IF-LL model. The model is divided into submodels, each of which has a subsection devoted to it, as noted in the boxes. The formula symbols are introduced in the following subsections. The last section, Sect. 2.6, describes the calculation of the total lift coefficient and the wing root bending moment coefficient from the local coefficients. In addition, the algorithm is summarized in Algorithm 1 in the appendix for better understanding.

2.1 3D to 2D and 2D to 3D

The lifting line method ensures that for a swept wing with sweep angle φ the lift curve slope is decreased by the factor $\cos\varphi$ compared to an unswept wing. However, the angle of attack used in the 2D airfoil data is too small by a factor of $\cos\varphi$. Therefore, in order for the stall to occur at the correct angle of attack, the 2D angle of attack α_{2D} must be increased about the factor $1/\cos\varphi$ relative to the 3D angle

[1] Data available online at https://github.com/iff-gsc/LADAC.

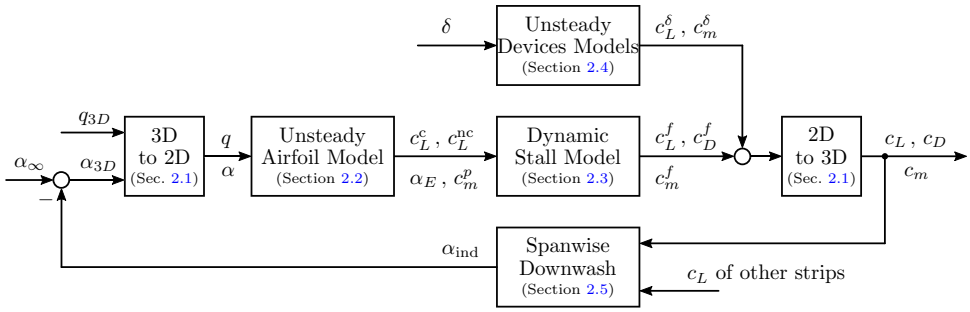

Fig. 1 Overview of nonlinear unsteady airfoil model with spanwise downwash coupling. The index i of all variables has been omitted for simplicity

of attack α_{3D}. Furthermore, however, it should be noted here that there is a special characteristic of stall in swept wings along the span [31]. Typically, the local maximum lift coefficient increases steadily from the wing tip to the wing root. This course of the maximum lift coefficient over the span depends on parameters such as sweep angle, aspect ratio and Mach number. This characteristic could be taken into account here empirically via a factor $f_{c_{L,\max}}$ dependent on the span position, which indicates the ratio between local maximum lift coefficient and the maximum lift coefficient of the airfoil used. The 2D airfoil angle of attack is consequently calculated as follows:

$$\alpha_{2D} = \alpha = (\alpha_{3D} - \alpha_0)/\left(\cos\varphi f_{c_{L,\max}}\right) + \alpha_0 \tag{1}$$

where α_0 is the angle of attack at zero lift. The 2D angle of attack α_{2D} will be denoted by α in the further course. The dimensionless pitch rate is defined as [18]

$$q = \dot{\alpha}c/V \tag{2}$$

with the airfoil chord length c and the airspeed V. The manipulation factor of the 2D angle of attack compared to the 3D angle of attack must be compensated at the end of the 2D calculations. For this purpose, the 3D coefficients are manipulated by the inverse factor compared to the 2D coefficients:

$$c_{L,3D} = c_L = \left(c_L^f + c_L^\delta\right)\cos\varphi f_{c_{L,\max}} \tag{3}$$

$$c_{m,3D} = c_m = \left(c_m^f + c_m^\delta\right)\cos\varphi f_{c_{L,\max}} \tag{4}$$

$$c_{D,3D} = c_D = c_D^f \cos\varphi f_{c_{L,\max}} \tag{5}$$

The 2D model also uses velocity V, Mach number M, and chord length c as parameters (denoted without index 2D in this work). These 2D parameters must also be changed compared to the 3D parameters:

$$V = V_\infty \cos\varphi \tag{6}$$

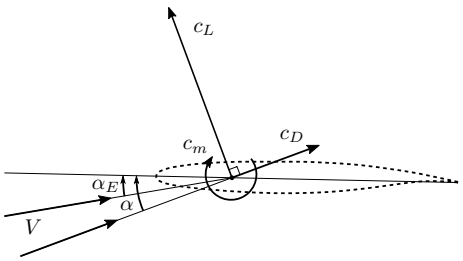

Fig. 2 Definition of airfoil inflow and coefficients

$$M = M_\infty \cos\varphi_{50\%} \tag{7}$$

$$c = c_{3D}/\cos\varphi \tag{8}$$

where V_∞ is the 3D velocity, M_∞ is the 3D Mach number and c_{3D} is the 3D chord (measured parallel to the fuselage). In this work, it has been found that the best results are obtained when correcting the 2D Mach number with the mean sweep angle of the 50% chord line $\varphi_{50\%}$.

2.2 Unsteady airfoil model

We use the unsteady 2D airfoil aerodynamics model for compressible flow from Leishman and Nguyen [18]. The definition of the incident flow and the aerodynamic coefficients is shown in Fig. 2. Due to a dynamic change of the angle of attack α, there is an effective angle of attack α_E, which is delayed with respect to the angle of attack. The drag coefficient acts in the direction of the free flow, the lift coefficient acts perpendicular to it. The reference point of the pitching moment coefficient is at the 25% point of the chord length.

The input variables to the unsteady airfoil model are the angle of attack α and the dimensionless pitch rate q. Furthermore, the model contains eight state variables $x_1, x_2, \ldots, x_8$, which represent first order delays of the input variables [18]:

$$\dot{x}_1 = \frac{1}{c/(2V\beta^2 b_1)}\left(\alpha - \alpha_0 + 0.5q - x_1\right) \tag{9}$$

Table 1 Unsteady airfoil aerodynamic parameters

A_1	A_2	A_3	A_4	b_1	b_2	b_3	b_4	b_5	κ_1	κ_2
0.625	0.375	1.5	−0.5	0.310	0.312	0.25	0.1	0.5	0.85	0.73

$$\dot{x}_2 = \frac{1}{c/\left(2V\beta^2 b_2\right)}\left(\alpha - \alpha_0 + 0.5q - x_2\right) \tag{10}$$

$$\dot{x}_3 = \frac{1}{K_\alpha T_I}\left(\alpha - \alpha_0 - x_3\right) \tag{11}$$

$$\dot{x}_4 = \frac{1}{K_q T_I}\left(q - x_4\right) \tag{12}$$

$$\dot{x}_5 = \frac{1}{b_3 K_{\alpha_M} T_I}\left(\alpha - \alpha_0 - x_5\right) \tag{13}$$

$$\dot{x}_6 = \frac{1}{b_4 K_{\alpha_M} T_I}\left(\alpha - \alpha_0 - x_6\right) \tag{14}$$

$$\dot{x}_7 = \frac{1}{c/(2V\beta^2 b_5)}\left(q - x_7\right) \tag{15}$$

$$\dot{x}_8 = \frac{1}{K_{q_M} T_I}\left(q - x_8\right) \tag{16}$$

with the Prandtl–Glauert factor

$$\beta = \sqrt{1 - M^2} \tag{17}$$

and time constants depending on Mach number [18]:

$$K_\alpha = \frac{\kappa_1}{1 - M + \pi\beta M^2\left(A_1 b_1 + A_2 b_2\right)} \tag{18}$$

$$K_q = \frac{\kappa_2}{1 - M + 2\pi\beta M^2\left(A_1 b_1 + A_2 b_2\right)} \tag{19}$$

$$T_I = c/a \tag{20}$$

$$K_{\alpha_M} = \frac{A_3 b_4 + A_4 b_3}{b_3 b_4 (1 - M)} \tag{21}$$

$$K_{q_M} = \frac{7}{15(1 - M) + 3\pi\beta M^2 b_5} \tag{22}$$

with the speed of sound a. The tunable parameters in the equations are defined in Table 1.

Finally, the model outputs of the unsteady airfoil model can be computed [18]:

$$\alpha_E = A_1 x_1 + A_2 x_2 \tag{23}$$

$$c_L^{\mathrm{c}} = c_{L\alpha}\alpha_E \tag{24}$$

$$c_L^{\mathrm{nc}} = \frac{4}{M}\left(\alpha - x_3\right) + \frac{1}{M}\left(q - x_4\right) \tag{25}$$

$$c_m^{\mathrm{c}} = c_L^{\mathrm{c}}\left(0.25 - x_{\mathrm{ac}}\right) - \frac{\pi}{8\beta}x_7 \tag{26}$$

$$c_m^{\mathrm{nc}} = \frac{1}{M}\left(A_3 x_5 + A_4 x_6 - \alpha\right) - \frac{7}{12M}\left(q - x_8\right) \tag{27}$$

where α_E is the effective angle of attack, $c_{L\alpha}$ is the lift curve slope, c_L^{c} is the circulatory part of the lift coefficient, c_L^{nc} is the non-circulatory part of the lift coefficient, c_m^{c} is the circulatory part of the pitching moment coefficient and c_m^{nc} is the non-circulatory part of the pitching moment coefficient. In Eq. (26), x_{ac} is the dimensionless aerodynamic center relative to the chord length. When coupled with the dynamic stall model, $x_{\mathrm{ac}} = 0.25$.

2.3 Dynamic stall model

Leishman and Beddoes (B–L) extended the unsteady 2D airfoil model from Sect. 2.2 to account for dynamic stall [16]. The B–L model includes trailing edge separation as well as leading edge separation. Since for the studies in this work, no distinct leading edge separation was apparent, we omitted the leading edge separation. For the drag coefficient, we made a few changes to the B–L model according to Hansen et al. [17] to get better validation results. The model extension about dynamic stall requires static analytic functions of the aerodynamic coefficients as shown in Fig. 3. The data points needed for this purpose were obtained in this work by steady-state RANS simulations. To improve the database, auxiliary points for small angles of attack are generated by linear extrapolation. To obtain an analytical model from the data points, a suitable function must first be selected. The function for the static lift coefficient c_L^{st} used in [16] has a kink and leads to quite large approximation errors with the present airfoil. The function from [32] also leads to large approximation errors, since it cannot represent a relative sharp change in lift coefficient during stall followed by relatively long almost linear decrease (occurs primarily at $M = 0.669$ and $M = 0.746$). Therefore, we modified the

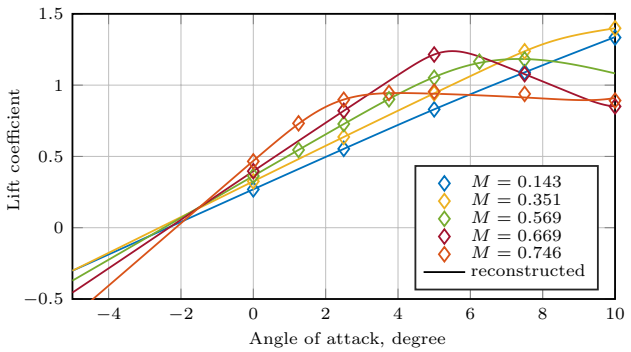

Fig. 3 Steady F15 airfoil lift coefficient model based on steady RANS data for multiple Mach numbers [30]

Table 2 Parameters of analytic lift coefficient reconstruction for the F15 airfoil obtained by curve fit

M	$\alpha_0/°$	$c_{L\alpha 0}$	$\Delta c_L^{\text{stall}}$	$\alpha^*/°$	a_1
0.143	− 2.358	6.484	− 0.030	9.599	6.502
0.351	− 2.595	6.736	− 0.249	11.56	8.667
0.569	− 2.472	6.930	− 1.457	13.88	3.882
0.669	− 2.329	7.262	− 0.637	7.766	11.81
0.746	− 2.144	8.358	− 0.909	6.365	6.938

function from [32]. We have replaced the $\tanh(a_1(\alpha - \alpha^*))$ function by a function with a sharper curvature $\tanh(\bar{\alpha})$ [30]:

$$c_L^{\text{st}} = \frac{c_{L\alpha 0}}{\beta} \sin\left(\alpha - \alpha_0\right) + \Delta c_L^{\text{stall}}[1 + \tanh\left(\bar{\alpha}\right)] \tag{28}$$

with

$$\bar{\alpha} = \sum_{i=1}^{3} \frac{\left(a_1(\alpha - \alpha^*)\right)^{(2i-1)}}{(2i-1)} \tag{29}$$

In Eq. (28), α_0 is the angle of attack at zero lift coefficient, $c_{L\alpha 0}$ is the lift curve slope at α_0 without compressibility correction, $\Delta c_L^{\text{stall}}$ is the magnitude of stall lift coefficient loss (negative), α^* is the angle of attack at which the stall magnitude is haft reached, and a_1 is the abruptness factor of the stall onset. The parameters were optimized using Matlab's nonlinear least-squares solver `lsqcurvefit` with the start points $\alpha_0 = -2°$, $c_{L\alpha 0} = 6.3$, $\Delta c_L^{\text{stall}} = 0$, $\alpha^* = 7°$, $a_1 = 5/°$ and with the boundary conditions $-7° \le \alpha_0 \le 7°$, $1.7 \le c_{L\alpha 0} \le 17$, $-1.5 \le \Delta c_L^{\text{stall}} \le 0$, $4° \le \alpha^* \le 30°$ and $0.2/° \le a_1 \le 20/°$. The results are shown in Table 2.

The dynamic stall model considers trailing edge flow separation. For this purpose, the dimensionless separation point f is defined, which is shown in Fig. 4. For fully attached flow, $f = 1$ and for fully detached flow, $f = 0$. The separation point can be obtained from the given static analytical lift coefficient function c_L^{st} [17]:

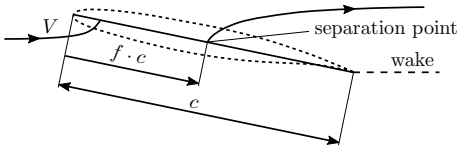

Fig. 4 Trailing edge separation point defined in the Kirchhoff flow past a flat plate according to [17]

$$f^{\text{st}}(\alpha) = \left(2\sqrt{\frac{c_L^{\text{st}}(\alpha)}{c_{L\alpha}(\alpha - \alpha_0)}} - 1\right)^2 \tag{30}$$

In Eq. (30), division by zero must be avoided. For this purpose, f is set to 1 for angles of attack of approximately α_0. Since $f \le 1$ applies, the lift curve slope $c_{L\alpha}$ in Eq. (30) is defined as [17]:

$$c_{L\alpha} = \max\left(c_L^{\text{st}}(\alpha)/(\alpha - \alpha_0)\right) \tag{31}$$

To represent the dynamics of the stall, a new state x_9 is introduced that represents a delay of the circulatory lift coefficient c_L^{c} [16]:

$$\dot{x}_9 = \frac{1}{T_p c/(2V)}\left(c_L^{\text{c}} + c_L^{\text{nc}} - x_9\right) \tag{32}$$

where T_p is a dimensionless time constant, which is selected to be $T_p = 1.7$ in this work. The delayed circulatory lift coefficient [16]

$$c_L' = x_9 \tag{33}$$

is used to calculate an angle of attack that would result in this quasi-steady lift coefficient if the lift curve were linear [16]:

$$\alpha^f = c_L'/c_{L\alpha} + \alpha_0 \tag{34}$$

For this angle of attack the corresponding quasi-steady separation point according to Eq. (30) can be obtained [16]:

$$f' = f^{\text{st}}\left(\alpha^f\right) \tag{35}$$

Another state x_{10} is introduced which represents a delay of this separation point [16]:

$$\dot{x}_{10} = \frac{1}{T_f c/(2V)}\left(f' - x_{10}\right) \tag{36}$$

where T_f is a dimensionless time constant, which is selected to be $T_f = 3$ in this work. Finally, from the delayed separation point [16]

$$f'' = x_{10} \tag{37}$$

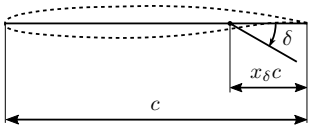

Fig. 5 Definition of flap geometry

the lift coefficient considering trailing edge flow separation can be obtained [16]:

$$c_L^f = c_{L\alpha}\left(\frac{1+\sqrt{f''}}{2}\right)^2 \cos\alpha_E + c_L^{\mathrm{nc}} \tag{38}$$

Good results for the drag coefficient were obtained using the method of [17]:

$$c_D^f = \left(c_L^f - c_L^{\mathrm{st}}\right)\sin\alpha + c_D^{\mathrm{st}} \tag{39}$$

where c_D^{st} is the static drag coefficient. Good results for the pitching moment coefficient were obtained using the method of [16]:

$$c_m^f = c_m^{\mathrm{st}} + \left[K_0 + K_1(1-f) + K_2\sin\left(\pi f^m\right)\right]c_L^f \tag{40}$$

where K_0, K_1, K_2 and m can be adjusted for different airfoils and Mach numbers [16]. For this purpose, optimization can be used as in the calculation of the parameters of the steady-state lift coefficient function in Eq. (28).

2.4 Unsteady devices models

This section describes the unsteady 2D aerodynamics of control devices. At this point, any and also multiple control devices are conceivable. However, we limit ourselves here to trailing-edge flaps, which are typically installed on wings.[2]

A relative flap depth x_δ is defined to each wing strip as shown in Fig. 5. The downward positive flap deflection is denoted by δ.

We use the linear potential-theoretic model for unsteady flap aerodynamics from [33]. This includes two state variables z_1 and z_2 for the modeling of the circulatory part of the lift coefficient. The state equation is [33]:

$$\begin{bmatrix}\dot{z}_1\\ \dot{z}_2\end{bmatrix} = \begin{bmatrix}0 & 1\\ -b_1b_2(2V/c)^2\beta^4 & -(b_1+b_2)(2V/c)\beta^2\end{bmatrix}\begin{bmatrix}z_1\\ z_2\end{bmatrix} + \begin{bmatrix}0\\ 1\end{bmatrix}\delta_{\mathrm{qs}} \tag{41}$$

For the non-circulatory part, two further states would be necessary, which, however, only play a significant role at very high flap dynamics. In Eq. (41), δ_{qs} is the quasi-stationary flap deflection depending on the flap deflection δ, its time derivative and the local flap hinge sweep angle φ_δ (i.e. the flap deflection is converted into a corresponding angle of attack) [33]:

$$\delta_{\mathrm{qs}} = \left(\frac{F_{10}}{\pi}\delta + \frac{F_{11}c}{4\pi V}\dot{\delta}\right)\cos\varphi_\delta \tag{42}$$

In Eq. (42), F_{10} and F_{11} are geometric quantities defined as follows [33]:

$$F_{10} = \sqrt{1-e^2} + \arccos e \tag{43}$$

$$F_{11} = (1-2e)\arccos e + (1-e)\sqrt{1-e^2} \tag{44}$$

with

$$e = 1 - 2x_\delta \tag{45}$$

The lift coefficient due to flap deflection can be calculated from the states [33]:

$$c_L^\delta = 2\pi/\beta\left[(b_1b_2)(2V/c)^2\beta^4 \;\; \left(A_1b_1 + A_2b_2\right)(2V/c)\beta^2\right]\begin{bmatrix}z_1\\ z_2\end{bmatrix} \tag{46}$$

2.5 Spanwise downwash

This section describes the coupling of the spanwise aerodynamics of a wing that is discretized into multiple strips, each of whose aerodynamics is modeled using the 2D airfoil models described in the previous Sects. 2.2–2.4. For a wing, it should be noted that the spanwise distributed strips influence each other by an induced angle of attack. This induced angle of attack is realized in this work by a steady lifting line model. Since the proper correction of the Mach number via manipulation of the influence coefficients is quite laborious, this section is divided into two subsections. Section 2.5.1 describes the spanwise downwash model without proper Mach number correction. Mach number correction is then discussed in Sect. 2.5.2.

2.5.1 Basic model without Mach number correction

The effective angle of attack of the local wing segments along the span is manipulated by an induced angle of attack α_{ind} computed by a steady lifting line model similar to [20, 24]. With this correction, the unsteady aerodynamics model computes the same lift distribution as the steady lifting line model for steady-state cases. In the steady-state lifting line method, the wing is covered by

[2] For active gust load alleviation, leading-edge flaps can be used in addition to trailing-edge flaps to compensate for the torsional moment due to gust and trailing-edge flap deflection. This was also done in [8], the results of which are used for validation in Sect. 3. Since we could not find a simple unsteady 2D model for leading-edge flaps in the literature, we have omitted leading-edge flaps in this work.

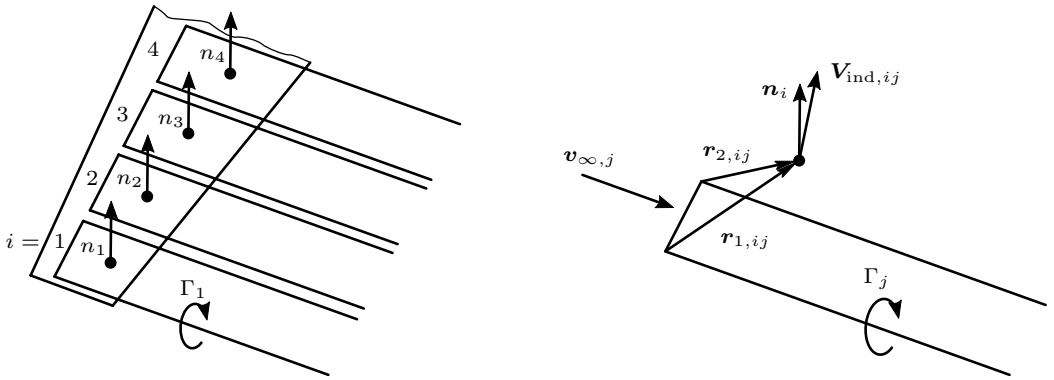

(a) Wing section with horseshoe vortex lattice model.

(b) Induced velocity due to a horseshoe vortex.

Fig. 6 Wing section with horseshoe vortex lattice model for solving the lifting-line problem based on [6]

horseshoe vortices of constant circulation Γ_i, see Fig. 6. The horseshoe vortices are placed on the 25% chord line and parallel to the incident flow. The control points are located on the 75% chord line.

First, the circulation associated with the previously calculated lift coefficients is calculated for all strips $i \in [\,1...N\,]$ along the span:

$$\Gamma_i = \frac{1}{2} V_\infty c^c_{L,i} c_i \tag{47}$$

The circulation can be used to determine the induced velocity at the control points caused by the circulation. The induced velocity at control point i by a single horseshoe vortex j of constant circulation Γ_j can be calculated with [34]:

$$\begin{aligned}\boldsymbol{V}_{\mathrm{ind},ij} = \frac{\Gamma_j}{4\pi}\Bigg(&\frac{\boldsymbol{v}_{\infty,j}\times\boldsymbol{r}_{2,ij}}{r_{2,ij}\left(r_{2,ij}-\boldsymbol{v}_{\infty,j}\cdot\boldsymbol{r}_{2,ij}\right)} + \frac{\left(r_{1,ij}+r_{2,ij}\right)\left(\boldsymbol{r}_{1,ij}\times\boldsymbol{r}_{2,ij}\right)}{r_{1,ij}r_{2,ij}\left(r_{1,ij}r_{2,ij}+\boldsymbol{r}_{1,ij}\cdot\boldsymbol{r}_{2,ij}\right)} \\ &- \frac{\boldsymbol{v}_{\infty,j}\times\boldsymbol{r}_{1,ij}}{r_{1,ij}\left(r_{1,ij}-\boldsymbol{v}_{\infty,j}\cdot\boldsymbol{r}_{1,ij}\right)}\Bigg) \\ = \boldsymbol{v}_{\mathrm{ind},ij}&\Gamma_j\end{aligned} \tag{48}$$

Here $\boldsymbol{r}_{1,ij}$ is the position vector from the left corner of the horseshoe vortex j to the control point i and $\boldsymbol{r}_{2,ij}$ is the position vector from the right corner of the horseshoe vortex j to the control point i, see Fig. 6B. The scalars $r_{1,ij} = |\boldsymbol{r}_{1,ij}|$ and $r_{2,ij} = |\boldsymbol{r}_{2,ij}|$ are the absolute values of the position vectors. $\boldsymbol{v}_{\infty,j}$ is the unit vector in the direction of the inflow at strip j. The boundary condition requires that the flow at all control points has no velocity in the direction of the normal vector of the strip [6]. That is, the sum of the induced velocities of all horseshoe vortices in the direction of the normal vectors together with the incident flow in the direction of the normal vectors equals zero [6]:

$$\boldsymbol{V}_i \cdot \boldsymbol{n}_i = \left(\boldsymbol{V}_{\infty,i} + \sum_{j=1}^{N} \boldsymbol{v}_{\mathrm{ind},ij}\Gamma_j\right)\cdot\boldsymbol{n}_i = 0 \tag{49}$$

Eq. (49) can be simplified by using the definition of the so-called influence coefficients matrix [6]

$$A_{ij} = \boldsymbol{v}_{\mathrm{ind},ij}\cdot\boldsymbol{n}_i \tag{50}$$

and by the scalar inflow velocity in direction of the normal vector

$$V_{n,i} = \boldsymbol{V}_{\infty,i}\cdot\boldsymbol{n}_i \tag{51}$$

so that Eq. (49) becomes:

$$\boldsymbol{V}_n = -\boldsymbol{A}\boldsymbol{\Gamma} \tag{52}$$

Since the inflow $V_{n,i}$ is known for each strip i, the corresponding inflow angle of attack of the lifting line model can be calculated:

$$\alpha_{ll,i} = \arcsin\left(\frac{V_{n,i}}{V_{\infty,i}}\right) \tag{53}$$

The corresponding expected lift coefficient from the nonlinear airfoil data without any spanwise downwash

$$c_{L,\infty,i} = 2\pi\alpha_{ll,i} \tag{54}$$

is used to compute the necessary induced angle of attack of each strip

$$\bar{\alpha}_{\mathrm{ind},i} = \frac{c_{L,\infty,i} - c^c_{L,i}}{2\pi} \tag{55}$$

This induced angle of attack for each strip $\bar{\alpha}_{\mathrm{ind},i}$ is subtracted from the inflow angle of attack $\alpha_{\infty,i}$, see Fig. 1:

$$\alpha_{3D,i} = \alpha_{\infty,i} - \alpha_{\mathrm{ind},i} \tag{56}$$

This adjusts the angle of attack α_i of the unsteady airfoil model. To avoid iterations at each time step, the calculated induced angle of attack is filtered with a first-order low pass filter:

$$\dot{\alpha}_{\mathrm{ind},i} = \frac{1}{T_{\mathrm{dw}}}\left(\bar{\alpha}_{\mathrm{ind},i} - \alpha_{\mathrm{ind},i}\right) \tag{57}$$

If the time constant T_{dw} is small enough, this method converges against the iterative solution, but has the advantages that the model is smooth and less computationally intensive.

It should be pointed out at this point that the spanwise course of the lift coefficient with this method shows slight oscillations during stall. The problem can be easily eliminated by a further spanwise coupling. According to Eq. (58)

$$\Delta\dot{x}_{10,i} = K_f\left(2x_{10,i} - x_{10,i-1} - x_{10,i+1}\right) \tag{58}$$

the time derivative of $x_{10,i}$ is extended by an increment $\Delta\dot{x}_{10,i}$ which is to be added to the result from Eq. (36). This allows a smooth course of the trailing edge separation point to be achieved. The factor K_f should be chosen as small as possible and so that the oscillations just disappear.

2.5.2 Mach number correction

Mach number leads to an increase in the lift curve slope of the airfoil in the transonic region, as can be seen from Eq. (17), Eq. (28) and Fig. 3. However, to correctly account for the influence on the spanwise lift distribution, an adjustment of the influence coefficients, see Eq. (50), must be made [6]. The wing depth must be increased by a factor of $1/\beta$, see Eq. (17). For this, the horseshoe vortices keep their original position, but the control points are shifted backwards. We call the Mach number corrected influence coefficients matrix $\boldsymbol{A}_M$. We note that if only a Mach-number-dependent 2D airfoil lift curve slope is used instead of an influence coefficients correction, this will result in an incorrect spanwise lift distribution.

However, there is now a problem with the Mach number correction of the influence coefficients, because a Mach-number-dependent lift curve slope, see Eq. (28), is also coupled in via the airfoil data. Thus, an influence coefficient matrix $\tilde{\boldsymbol{A}}_M$ must be found for which the Mach-number-corrected lift distribution is established when Mach-number-dependent lift curve slopes are used simultaneously. For this purpose, the model for the local lift coefficients is first linearized so that an analytical equation is obtained for the local lift coefficients. We use Eqs. (47), (51), (52), (53), (54), (55) and (57), where $\dot{\alpha}_{\mathrm{ind},i} = 0$ for a stationary result, and Eq. (53) is linearized: $\alpha_{ll,i} \approx V_{n,i}/V_{\infty,i}$. Moreover, we use a linear function for the lift coefficient: $c^{\mathrm{c}}_{L,i} = c_{L\alpha,i}\left(\alpha_i - \alpha_{0,i}\right)$, where $c_{L\alpha,i}$ is the local lift curve slope and $\alpha_{0,i}$ is the local zero lift angle of attack. If now all local variables with index i are bundled into vectors, e.g. $\boldsymbol{c}_{L\alpha} = [\, c_{L\alpha,1} \;\ldots\; c_{L\alpha,N} \,]^T$, $\boldsymbol{c} = [\, c_1 \;\ldots\; c_N \,]^T$, the analytical lift coefficient can be calculated from above equations:

$$\boldsymbol{c}_L = \boldsymbol{C}_{L\alpha}\left(\boldsymbol{\alpha}_\infty - \boldsymbol{\alpha}_0\right) \tag{59}$$

with the lift curve slope matrix $\boldsymbol{C}_{L\alpha} \in \mathbb{R}^{N\times N}$

$$\begin{aligned}\boldsymbol{C}_{L\alpha}\left(\boldsymbol{c}_{L\alpha}, \boldsymbol{A}\right) = {} & \operatorname{diag}\left(2\pi\boldsymbol{c}_{L\alpha}\right) \\ & \times \left[\operatorname{diag}\left(\boldsymbol{c}_{L\alpha}\right) - (2\pi\boldsymbol{E}) - \boldsymbol{A}\operatorname{diag}\left(\boldsymbol{c}_{L\alpha}\right)(\pi\boldsymbol{E})\operatorname{diag}(\boldsymbol{c})\right]^{-1}\end{aligned} \tag{60}$$

where $\boldsymbol{E} \in \mathbb{R}^{N\times N}$ is the identity matrix. In Eq. (60), the lift curve slope matrix $\boldsymbol{C}_{L\alpha}$ depends on the local lift curve slope vector $\boldsymbol{c}_{L\alpha}$ and the influence coefficients matrix $\boldsymbol{A}$. The correct spanwise lift distribution is obtained when $\boldsymbol{c}_{L\alpha} = \boldsymbol{c}_{L\alpha 0}$ and $\boldsymbol{A} = \boldsymbol{A}_M$, where $\boldsymbol{c}_{L\alpha 0}$ is the airfoil lift curve slope without compressibility correction, see Eq. (28), and $\boldsymbol{A}_M$ is the Mach number corrected influence coefficients matrix, see above. If one wishes to obtain the same lift distribution when $\boldsymbol{c}_{L\alpha} = \boldsymbol{c}_{L\alpha 0}/\beta$ is used as the airfoil lift curve slope, the following relation applies:

$$\boldsymbol{C}_{L\alpha}\left(\boldsymbol{c}_{L\alpha} = \boldsymbol{c}_{L\alpha 0}, \boldsymbol{A} = \boldsymbol{A}_M\right) := \boldsymbol{C}_{L\alpha}\left(\boldsymbol{c}_{L\alpha} = \boldsymbol{c}_{L\alpha 0}/\beta, \boldsymbol{A} = \tilde{\boldsymbol{A}}_M\right) \tag{61}$$

where $\tilde{\boldsymbol{A}}_M$ is the influence coefficient matrix we are looking for. Equation (61) solved for $\tilde{\boldsymbol{A}}_M$ gives

$$\begin{aligned}\tilde{\boldsymbol{A}}_M = {} & \left[\boldsymbol{A}_M\operatorname{diag}(\boldsymbol{\beta})\operatorname{diag}(\boldsymbol{c})\operatorname{diag}\left(\boldsymbol{c}_{L\alpha 0}\right) - 2\operatorname{diag}(\boldsymbol{\beta}) + 2\boldsymbol{E}\right] \\ & \times \left[\operatorname{diag}(\boldsymbol{\beta})\operatorname{diag}(\boldsymbol{c})\operatorname{diag}\left(\boldsymbol{c}_{L\alpha 0}\right)\right]^{-1}\end{aligned} \tag{62}$$

2.6 Total coefficients

The total coefficients can be determined by integrating the local coefficients. Since the wing was discretized into strips, the total coefficients can be calculated by summation. Since we assume small angles of attack, only the local lift coefficients can be used when calculating the total lift coefficient and the wing root bending moment coefficient. For the total lift coefficient

$$C_L = \frac{1}{S}\sum_{i=1}^{N} c_{L,i}c_i\Delta y_i \tag{63}$$

the local lift coefficients are multiplied by the area of the strip, where Δy_i is the width of the ith strip, and divided by the reference area S. The wing root bending moment is often used as a performance quantity in load reduction systems. In combination with the total lift, it also provides information on the spanwise lift distribution. The wing root bending moment coefficient for the right wing is calculated as follows:

Table 3 Main geometrical parameters of the LEISA configuration

Span	Aspect ratio	Taper ratio	Leading edge sweep	Twist	Dihedral
40 m	9.14	0.20	30°	−0.86°	5.0°

$$C_{\mathrm{WRBM}} = \frac{1}{S/2} \sum_{i=N/2+1}^{N} c_{L,i} c_i \Delta y_i (\eta_i - \eta_{\mathrm{root}}) b_i \tag{64}$$

where $-1 \leq \eta_i \leq 1$ is the dimensionless span coordinate of the i-th strip, η_{root} is the dimensionless span coordinate of the wing root, and b_i is a boolean variable to consider only strips outside η_{root}:

$$b_i = \begin{cases} 1 \text{ if } \eta_i - \eta_{\mathrm{root}} > 0 \\ 0 \text{ otherwise} \end{cases} \tag{65}$$

3 Validation

In this section, the reduced-order NL-IF-LL model presented in Sect. 2 is compared with URANS models. The results from the URANS simulations are taken from [7, 8, 29]. For details on the URANS models, please refer to these publications.

Section 3.1 describes the airplane and the simulation scenario. Then, in Sect. 3.2, a validation of the 2D airfoil model is performed. Subsequently, gust loads for the 3D wing are validated in Sect. 3.3. Flap deflections are validated in Sect. 3.4. Finally, gust loads with simultaneous, dynamic flap deflections are validated in Sect. 3.5.

3.1 Airplane and simulation scenario

To study the aerodynamic model presented in Sect. 2, we apply it to the DLR aircraft "Leiser Start und Anflug" (LEISA), which is a short-to-medium range, single-aisle, twin-engine aircraft [35]. Figure 7a shows the RANS model geometry of the wing-fuselage configuration and illustrates the trailing edge setup for active load alleviation. The five spanwise-segmented flaps were designed for active control of maneuver and gust loads [8]. The transonic DLR-F15 airfoil is used as the reference airfoil of the wing. Table 3 shows the main geometric parameters of the LEISA wing.

Figure 7b shows the geometry of the NL-IF-LL model with 25% chord line and control points. A discretization of the wing in $N = 40$ strips was chosen. With the $N = 40$ strips, the NL-IF-LL model comes to a total of $40 \cdot 13 = 520$ states, per strip 10 for the unsteady airfoil aerodynamic states $\boldsymbol{x}_i$, 2 for the unsteady flap aerodynamics states $\boldsymbol{z}_i$ and 1 for the unsteady spanwise downwash angle of attack $\alpha_{\mathrm{ind},i}$. In the area of the fuselage the wing is continued. A time step size of 0.001 seconds and an Euler forward solver are chosen for the simulation.

Cruise flight is used as the operating point, which for the LEISA configuration is a lift coefficient of $C_L = 0.5$ at an altitude of 10668 m and a Mach number of $M_\infty = 0.8$. In the international standard atmosphere, this corresponds to an airspeed of $V_\infty = 237.2\,\mathrm{m/s}$. The wing root bending moment is calculated with respect to $\eta_{\mathrm{root}} = 0.1037$.

In the simulations of the F15 airfoil, there is a lift coefficient of $c_L = 0.656$, at an altitude of 10668 m and a Mach number of $M = 0.74$, which corresponds to an airspeed of $V = 219.4\,\mathrm{m/s}$.

The FAR25 and the CS25 describe all loads due to wind that must be considered [1, 2]. In this paper, discrete upward "1-cos" gusts of various lengths λ at cruise

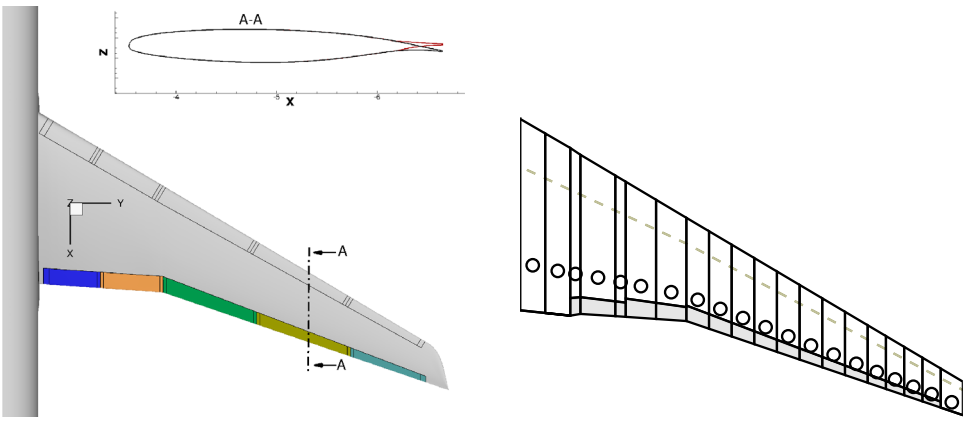

Fig. 7 LEISA configuration

(a) RANS geometry with illustration of segmented trailing-edge flaps.

(b) NL-IF-LL geometry.

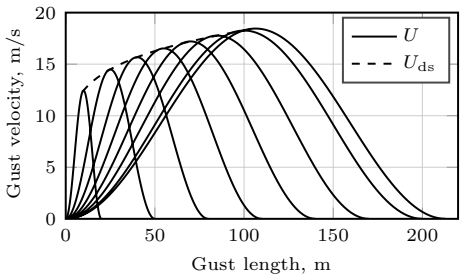

Fig. 8 1-cos design gust velocity profiles according to FAR25 and CS25

altitude, exactly as in [7, 8], are studied. The vertical gust velocity is defined as:

$$U = \begin{cases} \frac{U_{ds}}{2}\left(1 - \cos\left(\frac{2\pi x}{\lambda}\right)\right) & \text{if } 0 \le x \le \lambda, \\ 0 & \text{otherwise.} \end{cases} \tag{66}$$

with

$$U_{ds} = U_{ref} F_g \left(\frac{\lambda}{213.4\text{m}}\right)^{1/6}, \quad 18.29\text{m} \le \lambda \le 213.4\text{m} \tag{67}$$

where $x = \int V_\infty \mathrm{d}t$ is the gust penetration distance. The reference gust velocity U_{ref} and the flight profile alleviation factor F_g are functions of the flight altitude. At the selected altitude the reference gust velocity is given as $U_{ref} = 18.46\,\text{m/s}$. Conservatively, we assume that $F_g = 1$, which means that the aircraft operates always at the cruise altitude. The studied gusts are illustrated in Fig. 8.

We assume that the gust is constant in the lateral direction. Because of the wing sweep angle, it is taken into account that the gust reaches the wing strips with a time delay. The local angle of attack of the ith strip

$$\alpha_{\infty,i} = \arcsin\left(\frac{\boldsymbol{n}_i \cdot \left[V_\infty,\ 0,\ -U_i\right]^T}{\sqrt{V_\infty^2 + U_i^2}}\right) \tag{68}$$

where U_i is gust velocity at the ith strip and the vectors are represented in a forward-right-down coordinate system.

3.2 Airfoil

According to Fig. 1, the NL-IF-LL model includes a linear "unsteady airfoil model" and a nonlinear "dynamic stall model". For 2D airfoils, these models can be used independently. In this section, we refer to the linear "unsteady airfoil model" as the IF model and the linear "unsteady airfoil model" combined with the "dynamic stall model" as the NL-IF model. The URANS data in this section was obtained from [29].

Figure 9a shows a comparison of the lift coefficient of the IF model with the URANS model for three gust interactions. At the beginning and end of the gust, the lift coefficients are similar. However, there is a huge difference in the middle part. The linear IF model produces a course of the lift coefficient which qualitatively corresponds approximately to the course of the 1-cos gust. In the URANS simulation, stall occurs, so that the maximum lift coefficient is relatively low.

Figure 9b shows a comparison of the lift coefficient of the NL-IF model with the URANS model for the same three gusts as in Fig. 9a. The NL-IF model agrees much better with the URANS model than the IF model. Typical for the course of the lift coefficients is that the course is not symmetrical in contrast to the IF model. This is due to the fact that the flow separates with a delay during dynamic stall, which can lead to a short exceeding of the maximum stationary lift coefficient. The NL-IF model tends to reproduce the initial course of the lift coefficient better than the course during the decay of the gust. Moreover, the NL-IF model

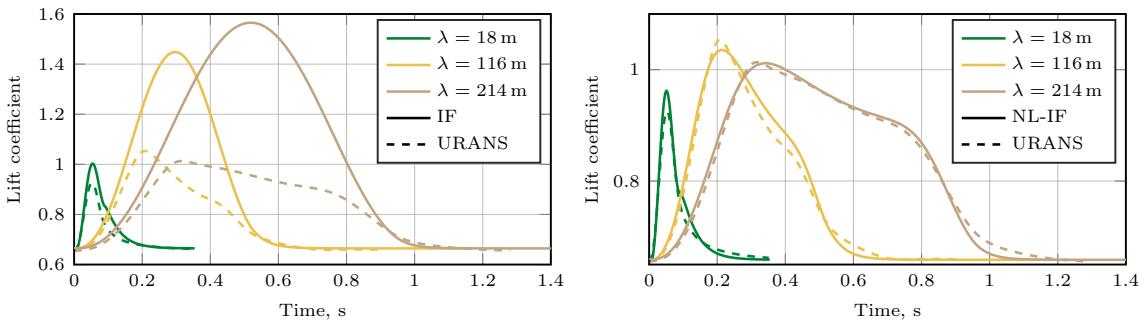

(a) IF model. (b) NL-IF model.

Fig. 9 Comparison of 2D linear indicial function (IF) model and nonlinear dynamic stall (NL-IF) model with URANS model for multiple gust wavelengths using the F15 airfoil

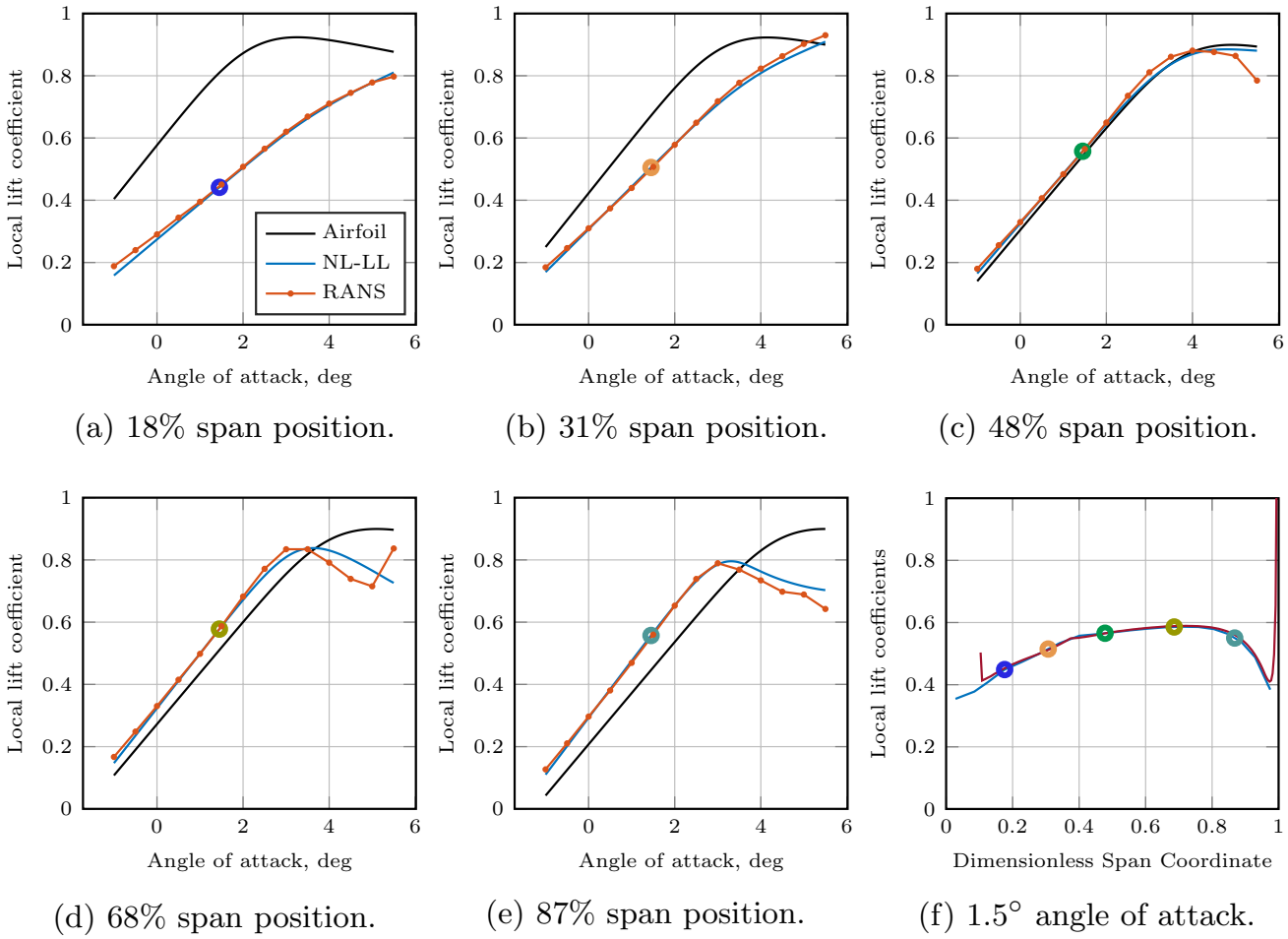

(a) 18% span position. (b) 31% span position. (c) 48% span position.

(d) 68% span position. (e) 87% span position. (f) 1.5° angle of attack.

Fig. 10 Local lift vs. angle of attack at five spanwise positions (**a**–**e**) and spanwise lift distribution in cruise (**f**) of the LEISA configuration

calculates a somewhat too large maximum lift coefficient for the shortest gust.

3.3 Wing

In this section, the NL-IF-LL model presented in Sect. 2 is validated for the 3D wing. In addition to the NL-IF-LL model, a variant with deactivated dynamic stall model is also used, which is called IF-LL accordingly. For a steady-state analysis of the wing model with stall, a variant with unsteady aerodynamics disabled is also used, which is denoted NL-LL in this section.

Figure 10 shows a steady-state validation of the NL-LL model. The RANS results were taken from [8]. The steady-state spanwise lift distribution in cruise is shown in Fig. 10f. Here, the colored circles indicate the spanwise position at which the local lift coefficients over the angle of attack are shown in Fig. 10a–e. It can be seen in Fig. 10a–e that the NL-LL local lift curve slopes below stall are in very good agreement with RANS results. For the NL-LL model, the maximum local lift coefficient in Fig. 10d and e without manipulation would be slightly higher at about 0.9, i.e., where the sweep-corrected airfoil also has its maximum lift. The manipulation leading to the earlier stall at the outer wing region was performed via the parameter $f_{c_{L,\max}}$ in Eq. (1). This scaling factor, which is 1 by default, was reduced to 0.85 towards the wing tip. Although the performance of the NL-LL model for steady-state stall is satisfactory, unfortunately the model does not include a semi-empirical determination of the parameter $f_{c_{L,\max}}$—so the parameter must be calibrated for each wing by experimental or simulative results.

In the next step, an interaction with a 1-cos gust of reduced strength is simulated. Figure 11 shows the comparison of the NL-IF-LL model, the IF-LL model and the URANS model. The URANS results were taken from [7]. Due to the reduced gust strength of $U_{\mathrm{ds}} = 10\,\mathrm{m/s}$ instead of $U_{\mathrm{ds}} = 14.49\,\mathrm{m/s}$, only very weak stall occurs in this scenario. The IF-LL model provides a slightly too high load because the weak stall is not taken into account. The NL-IF-LL model provides very accurate results. It can be seen from the good agreement of the wing root bending moment

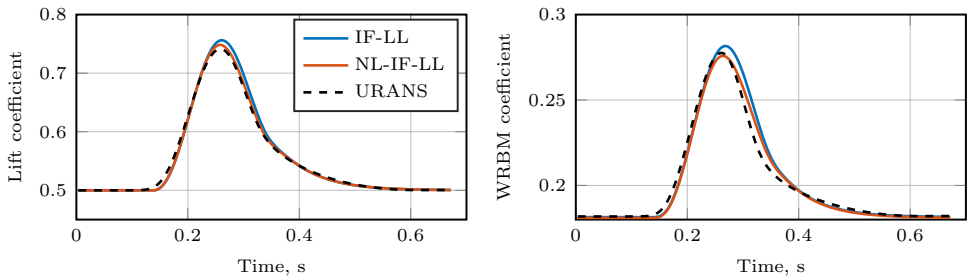

(a) Lift coefficient. (b) WRBM coefficient.

Fig. 11 Comparison of IF-LL and RANS for one gust ($\lambda = 50\,\text{m}, U_{\text{ds}} = 10\,\text{m/s}$) using the LEISA configuration

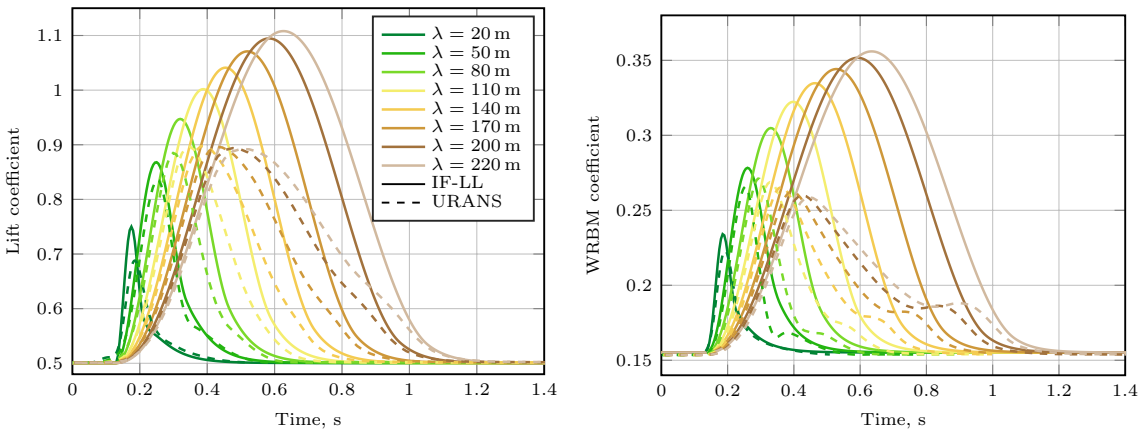

(a) Lift coefficient. (b) WRBM coefficient.

Fig. 12 Comparison of IF-LL (without dynamic stall model) and RANS for multiple gust wavelengths using the LEISA configuration

coefficient in Fig. 11b that the spanwise distribution of the lift also agrees well.

Figure 12 compares IF-LL model results for stronger gusts of various lengths, as shown in Fig. 8, with URANS results. It can be seen that the lift coefficient for the URANS model does not increase further from a gust length of about $\lambda = 110\,\text{m}$. This is due to the fact that strong flow separation occurs. For the wing root bending moment coefficient, the maximum even decreases for longer gusts. The IF-LL model does not take stall into account and delivers lift coefficients that are clearly too high, especially for the long, strong gusts. The highest occurring increase of the lift coefficient $\Delta C_{L,\max} = \max(C_L) - 0.5$ is about 50% too high. For the wing root bending moment coefficient, the highest occurring increase is even more than 60% too high.

Figure 13 shows the same simulations as Fig. 12, except that the IF-LL model has been replaced by the NL-IF-LL model. It can be seen that the NL-IF-LL model calculates significantly lower loads than the IF-LL model. For the lift coefficient, the largest deviations occur in the two shortest gusts. The maximum occurring value is too high. Apart from the two shortest gusts, the courses of the lift coefficients are satisfactory. For the wing root bending moment coefficient, there are larger deviations. This indicates that the spanwise lift distribution in the NL-IF-LL model is somewhat inaccurate. For the second and third shortest gusts, the maximum coefficients occurring are slightly too small. During decay, the coefficients are too high for all gusts. An analysis has shown that the dynamic stall occurs somewhat delayed at the wing tip. Subsequently, there is a stronger collapse of lift at the wing tip than can be explained by the 2D dynamic stall model. We were able to correct the static stall error caused by wing sweep with the correction factor $f_{c_{L,\max}}$ (see above). However, we suspect that there is also a dynamic characteristic that is not included in the model and is also caused by wing sweep. Nevertheless, the NL-IF-LL model is a significant improvement over the IF-LL model.

3.4 Flaps

In this section, the presented NL-IF-LL model is validated for trailing-edge flap deflections. For this purpose, the steady-state spanwise lift distribution due to individual static flap deflections are compared with RANS results in Fig. 14. Since there are no unsteady aerodynamics in this scenario and since there are no flow separations, the NL-IF-LL model reduces to a lifting-line model, called LL model. If the flaps are not deflected, it results in very well matched

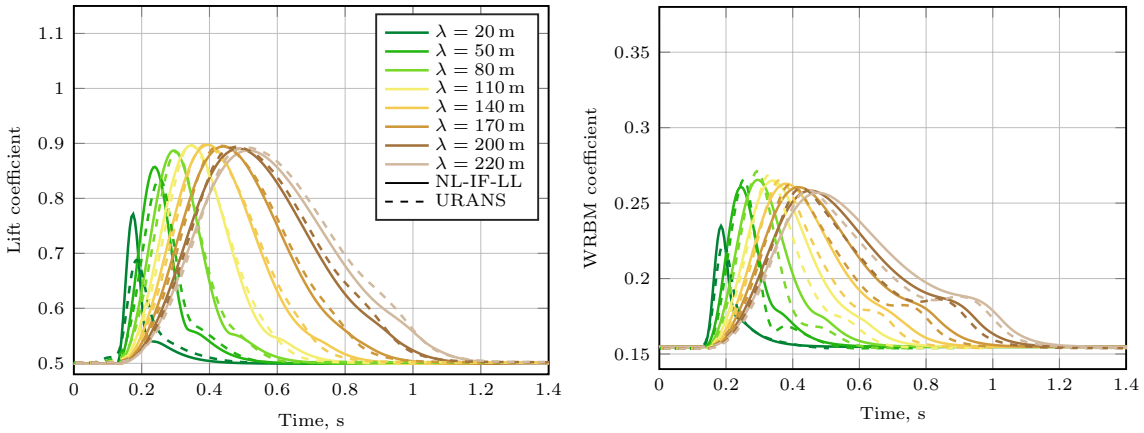

(a) Lift coefficient. (b) WRBM coefficient.

Fig. 13 Comparison of NL-IF-LL (with dynamic stall model) and URANS for multiple gust wavelengths using the LEISA configuration

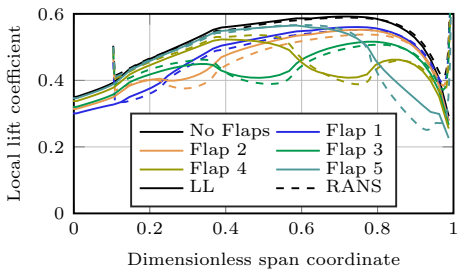

Fig. 14 Comparison of LL and RANS for steady spanwise lift distribution with single flap deflections of −8° using the LEISA configuration

spanwise distribution of the lift coefficient. In case of individual flap deflections, the courses differ more from each other. The total lift coefficient is very similar, but in the outer area of the wing the local lift coefficient is too high and in the inner area too low. This is mainly due to limitations of the LL model. Local lift due to trailing-edge flap deflection is applied at the 1/4 chord line in the LL model. In reality, however, the local lift is increased behind the 1/4 chord line. For a backward swept wing, the influence on the outer wing area is then higher than on the inner wing area.

Figure 15 shows results for dynamic trailing-edge flap deflections. Here, the trailing-edge flaps are deflected simultaneously as described in [8] so that they would approximately compensate for a 1-cos gust. Since no flow separations occur in this scenario, the NL-IF-LL model is referred to here as IF-LL. The course of the IF-LL model agrees quite well with the URANS simulations. However, when the flap deflection is reduced, the coefficients of the IF-LL model return to their original values somewhat faster. This error could possibly be reduced by a different choice of the IF model parameters, see Table 1.

3.5 Combined gust and flap deflections

In this section, the results of the NL-IF-LL model are validated for a gust encounter with simultaneous trailing edge deflection. The URANS results of this section were taken from [8]. In Fig. 16, the loads during the gust encounter (gust only) with $\lambda = 50$m are shown again as in Fig. 11. Furthermore, the loads are shown which result when the trailing-edge flaps are deflected in addition to the gust (gust + flaps), as described in the previous Sect. 3.4. In addition to the results of the full NL-IF-LL model, results with stall disabled, referred to as IF-LL, are shown. It can be seen that

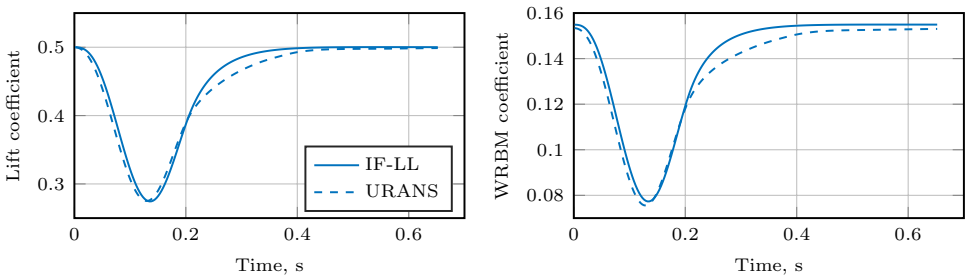

(a) Lift coefficient. (b) WRBM coefficient.

Fig. 15 Comparison of NL-IF-LL and URANS for simultaneous flap deflections corresponding to one gust with $\lambda = 50$ m and $U_{ds} = 14.49$ m/s using the LEISA configuration

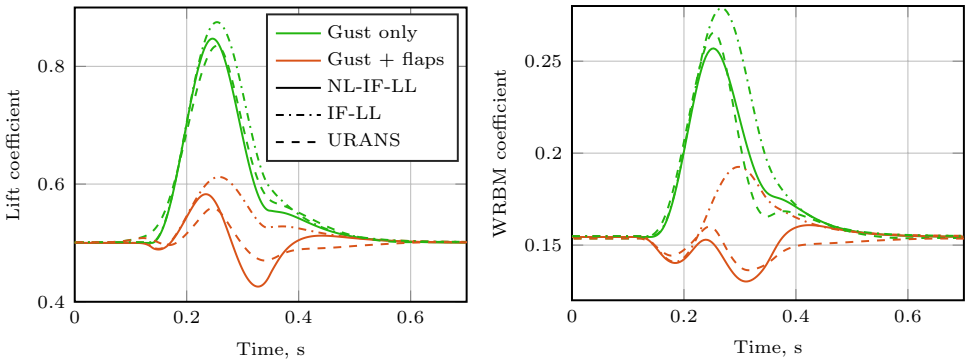

(a) Lift. (b) Wing root bending moment.

Fig. 16 Comparison of NL-IF-LL, IF-LL and URANS for gust response ($\lambda = 50\,\text{m}$, $U_{\text{ds}} = 14.49\,\text{m/s}$) with and without gust load alleviation using the LEISA configuration

the NL-IF-LL model calculates a significantly more accurate wing root bending moment than the IL-LL model. This is apparently due to the fact that stall occurs in the outer region of the wing even with flap deflection. Overall, the lift and wing root bending moment of the NL-IF-LL model are satisfactory. It should be noted that this is a complex scenario, so moderate deviations are not surprising.

4 Conclusions and limitations

Previously published, computationally expensive URANS simulations have shown that dynamic stall can reduce gust loads on commercial airplanes. However, it should be noted that the aircraft in these simulations was rigid and unaccelerated. In this paper, a novel physics-based, low-order wing model, NL-IF-LL, is presented that can also represent stall. The model represents a combination of indicial functions for unsteady 2D aerodynamics with a semi-empirical dynamic stall model and a lifting line model.

The NL-IF-LL model is compared to the URANS results for gust interactions. The gust loads are calculated much more accurately with the NL-IF-LL model than when the stall is neglected.

Moreover, the NL-IF-LL model is designed so that load alleviation devices can be integrated in a modular fashion. The implementation of load alleviation devices is described as an example for trailing-edge flaps.

Finally, the NL-IF-LL model is compared to URANS results for gust interactions with simultaneous dynamic trailing-edge flap deflection to compensate for the gust load. Here it can be seen that also in this scenario the consideration of the model for the dynamic stall achieves more accurate results than without this consideration. It follows that in the design and simulation of intensive gust load alleviation systems, where the assumption of a rigid and unaccelerated aircraft is approximately fulfilled, the consideration of dynamic stall may indeed be relevant.

The NL-IF-LL model has three main limitations from which future work can be derived: (1) One limitation concerns the modeling of the stall. It has been found that the static stall at the wing tip occurs earlier than would be expected from the maximum local airfoil lift coefficient (see Sect. 3.3 and Fig. 10). This effect can presumably be traced back to the sweep and could be easily corrected retrospectively via the parameter $f_{c_{L,\max}}$. However, there is still a mismatch for dynamic stall. In the URANS simulations, strong dynamic lift collapses occur at the wing tips due to stall, the strength of which cannot be explained and reproduced by the NL-IF-LL model. Therefore, the loads are still slightly wrong with the NL-IF-LL model (see Fig. 13b). We suspect that the strong dynamic stall at the wingtips is due to the backward sweep, because detachment regions could propagate backward and thus outward. This effect could be analyzed in the future using wings with different parameters to derive a reduced-order model for this purpose. (2) Another limitation is the spanwise lift distribution at local trailing-edge flap deflections. For swepts wings, the center of lift is slightly shifted inwards with the lifting line method (see Fig. 14). To avoid this, the model could be further developed in the future to discretize the wing in the depth direction so that trailing-edge flaps have their own panels. (3) The unsteady lift due to dynamic trailing-edge flap deflection returns to its original value somewhat too quickly (see Fig. 15). This could be improved by optimizing the parameters in Table 1. While the parameters in Table 1 fit well for the clean airfoil, they do not seem to be optimally suited for the trailing-edge flaps.

Appendix A: Nonlinear indicial function lifting line (NL-IF-LL) algorithm

Algorithm 1 Nonlinear indicial function lifting line (NL-IF-LL) algorithm

Algorithm 1 Nonlinear indicial function lifting line (NL-IF-LL) algorithm

Initialize geometry and aerodynamic influence coefficients
for Every spanwise strip i **do**
    Initialize all states: $\boldsymbol{x}_i = \boldsymbol{x}_{\text{init},i}$, $\boldsymbol{z}_i = \boldsymbol{z}_{\text{init},i}$, $\alpha_{\text{ind},i} = \alpha_{\text{ind,init},i}$
end for
for Each simulation time step **do**
    for Every spanwise stip i **do**
        Receive local 3D inflow: $\alpha_{\infty,i}$, q_i, $V_{\infty,i}$, $M_{\infty,i}$
        Compute 3D effective angle of attack, Fig. 1: $\alpha_{3D,i} = \alpha_{\infty,i} - \alpha_{\text{ind},i}$
        Transform 3D variables to 2D: Eqs. (1), (6), (7)
        Compute linear unsteady 2D airfoil state derivatives $\dot{x}_1$–$\dot{x}_8$, Eqs. (9)–(16), and outputs, Eqs. (24)–(28)
        Compute 2D dynamic stall state derivatives $\dot{x}_9$, $\dot{x}_{10}$, Eqs. (33), (37), and outputs, Eqs. (29)–(41)
        Transform 2D variables back to 3D, Eq. (5), to obtain the lift coefficient $c^{\text{c}}_{L,i}$
        Compute circulation, see Eq. (48): $\Gamma_i = \frac{1}{2} V_{\infty,i} c^{\text{c}}_{L,i} c_i$
    end for
    Compute LL velocity component normal to wing strips, Eq. (53): $\boldsymbol{V}_n = -\boldsymbol{A}\boldsymbol{\Gamma}$
    for Every spanwise strip i **do**
        Compute LL inflow angle of attack, Eq. (54): $\boldsymbol{\alpha}_{ll,i} = \arcsin(V_{n,i}/V_{\infty,i})$
        Compute LL lift coefficient without any downwash, Eq. (55): $c_{L,\infty,i} = 2\pi\alpha_{ll,i}$
        Compute corresponding steady-state induced angle of attack, Eq. (56): $\bar{\alpha}_{\text{ind},i} = (c_{L,\infty,i} - c^{\text{c}}_{L,i})/(2\pi)$
        Compute time-derivative of induced angle of attack, Eq. (58): $\dot{\alpha}_{\text{ind},i} = 1/T_{\text{dw}} \cdot (\bar{\alpha}_{\text{ind},i} - \alpha_{\text{ind},i})$
        Update all states $\boldsymbol{x}_i$, $\boldsymbol{z}_i$, $\alpha_{\text{ind},i}$
    end for
end for

Acknowledgements We would like to acknowledge the funding by the Deutsche Forschungsgemeinschaft (DFG, German Research Foundation) under Germany's Excellence Strategy—EXC 2163/1–Sustainable and Energy Efficient Aviation—Project-ID 390881007.

Funding Open Access funding enabled and organized by Projekt DEAL.

Data availability The datasets generated and analysed during the current study are available with restrictions from the corresponding author on reasonable request.

Declarations

Conflict of interest The authors have no conflict of interest to declare that are relevant to the content of this article.

Open Access This article is licensed under a Creative Commons Attribution 4.0 International License, which permits use, sharing, adaptation, distribution and reproduction in any medium or format, as long as you give appropriate credit to the original author(s) and the source, provide a link to the Creative Commons licence, and indicate if changes were made. The images or other third party material in this article are included in the article's Creative Commons licence, unless indicated otherwise in a credit line to the material. If material is not included in the article's Creative Commons licence and your intended use is not permitted by statutory regulation or exceeds the permitted use, you will need to obtain permission directly from the copyright holder. To view a copy of this licence, visit http://creativecommons.org/licenses/by/4.0/.

References

1. Airworthiness Standards.: Transport Category Airplanes. Federal Aviation Administration, U.S. Dept. of Transport. Chap. 25.341 (2024)
2. Certification Specifications and Acceptable Means of Compliance for Large Aeroplanes (CS-25).: European Aviation Safety Agency, Cologne. Chap. 25.341 (2021)
3. Dussart, G., Portapas, V., Pontillo, A., Lone, M.: Flight dynamic modelling and simulation of large flexible aircraft. In: Flight

Physics–models, Techniques and Technologies. IntechOpen, London (2018). https://doi.org/10.5772/intechopen.71050
4. Wu, Z., Cao, Y., Ismail, M.: Gust loads on aircraft. Aeronaut. J. **123**(1266), 1216–1274 (2019)
5. Reimer, L., Heinrich, R., Ritter, M.: Towards higher-precision maneuver and gust loads computations of aircraft: status of related features in the cfd-based multidisciplinary simulation environment flowsimulator. In: New Results in Numerical and Experimental Fluid Mechanics XII: Contributions to the 21st STAB/DGLR Symposium, Darmstadt, 2018, pp. 597–607. Springer (2020). https://doi.org/10.1007/978-3-030-25253-3_57
6. Katz, J., Plotkin, A.: Low-Speed Aerodynamics, vol. 13. Cambridge University Press, New York (2001). https://doi.org/10.1017/CBO9780511810329
7. Ullah, J., Lutz, T., Klug, L., Radespiel, R., Wild, J.: Active gust load alleviation by combined actuation of trailing edge and leading edge flap at transonic speeds. In: AIAA Scitech 2021 Forum, AIAA Paper 2021–1831 (2021). https://doi.org/10.2514/6.2021-1831
8. Ullah, J., Lutz, T., Klug, L., Radespiel, R., Wild, J., Heinrich, R.: Approach for aerodynamic gust load alleviation by means of spanwise-segmented flaps. J. Aircr. (2023). https://doi.org/10.2514/1.C037086
9. DeLaurier, J.D.: An aerodynamic model for flapping-wing flight. Aeronaut. J. **97**(964), 125–130 (1993). https://doi.org/10.1017/S0001924000026002
10. Andrews, S.P.: Modelling and simulation of flexible aircraft: handling qualities with active load control. PhD thesis, School of Engineering, Cranfield Univ., Cranfield, England (2011)
11. Silvestre, F.J., Luckner, R.: Experimental validation of a flight simulation model for slightly flexible aircraft. AIAA J. **53**(12), 3620–3636 (2015). https://doi.org/10.2514/1.J054023
12. Wang, X., Van Kampen, E., Chu, Q., De Breuker, R.: Flexible aircraft gust load alleviation with incremental nonlinear dynamic inversion. J. Guid. Control. Dyn. **42**(7), 1519–1536 (2019). https://doi.org/10.2514/1.G003980
13. Ritter, M., Teixeira, P., Cesnik, C.E.: Comparison of nonlinear aeroelastic methods for maneuver simulation of very flexible aircraft. In: 2018 AIAA/ASCE/AHS/ASC Structures, Structural Dynamics, and Materials Conference, AIAA Paper 2018-1953 (2018). https://doi.org/10.2514/6.2018-1953
14. Carrizales, M.A., Dussart, G., Portapas, V., Pontillo, A., Lone, M.: Verification of a low fidelity fast simulation framework through RANS simulations. CEAS Aeronaut. J. **11**(1), 161–176 (2020). https://doi.org/10.1007/s13272-019-00409-x
15. Kim, D.-K., Lee, J.-S., Lee, J.-Y., Han, J.-H.: An aeroelastic analysis of a flexible flapping wing using modified strip theory. In: Proceedings of SPIE, vol. 6928. Paper 69281O (2008). https://doi.org/10.1117/12.776137
16. Leishman, J.G., Beddoes, T.: A semi-empirical model for dynamic stall. J. Am. Helicopter Soc. **34**(3), 3–17 (1989). https://doi.org/10.4050/JAHS.34.3.3
17. Hansen, M.H., Gaunaa, M., Aagaard Madsen, H.: A Beddoes-Leishman Type Dynamic Stall Model in State-space and Indicial Formulations. Denmark. Forskningscenter Risoe. Risoe-R, vol. 1354(EN) (2004)
18. Leishman, J., Nguyen, K.: State-space representation of unsteady airfoil behavior. AIAA J. **28**(5), 836–844 (1990). https://doi.org/10.2514/3.25127
19. Barnes, J.: Semi-empirical vortex step method for the lift and induced drag loading of 2d or 3d wings. In: World Aviation Congress, AIAA Paper 975559 (1997). https://doi.org/10.2514/6.1997-5559
20. Van Dam, C.: The aerodynamic design of multi-element high-lift systems for transport airplanes. Prog. Aerosp. Sci. **38**(2), 101–144 (2002). https://doi.org/10.1016/S0376-0421(02)00002-7
21. Gallay, S., Laurendeau, E.: Nonlinear generalized lifting-line coupling algorithms for pre/poststall flows. AIAA J. **53**(7), 1784–1792 (2015). https://doi.org/10.2514/1.J053530
22. Gallay, S., Laurendeau, E.: Preliminary-design aerodynamic model for complex configurations using lifting-line coupling algorithm. J. Aircr. **53**(4), 1145–1159 (2016). https://doi.org/10.2514/1.C033460
23. Gamble, L.L., Pankonien, A.M., Inman, D.J.: Stall recovery of a morphing wing via extended nonlinear lifting-line theory. AIAA J. **55**(9), 2956–2963 (2017). https://doi.org/10.2514/1.J055042
24. Goitia, H., Llamas, R.: Nonlinear vortex lattice method for stall prediction. In: 9th EASN International Conference on "Innovation in Aviation & Space", vol. 304. MATEC Web Conf., Paper 02006 (2019). https://doi.org/10.1051/matecconf/201930402006
25. Weissinger, J.: The lift distribution of swept-back wings. National Advisory Committee for Aeronautics (1947)
26. Parenteau, M., Plante, F., Laurendeau, E., Costes, M.: Unsteady coupling algorithm for lifting-line methods. In: 55th AIAA Aerospace Sciences Meeting, AIAA Paper 2017-0951 (2017). https://doi.org/10.2514/6.2017-0951
27. Sugar-Gabor, O.: A general numerical unsteady non-linear lifting line model for engineering aerodynamics studies. Aeronaut. J. **122**(1254), 1199–1228 (2018). https://doi.org/10.1017/aer.2018.57
28. Dias, J.N.: Nonlinear lifting-line algorithm for unsteady and poststall conditions. In: 34th AIAA Applied Aerodynamics Conference, AIAA Paper 2016-4164 (2016). https://doi.org/10.2514/6.2016-4164
29. Asaro, S., Khalil, K., Bauknecht, A.: Unsteady characterization of fluidic flow control devices for gust load alleviation. In: New Results in Numerical and Experimental Fluid Mechanics XIII: Contributions to the 22nd STAB/DGLR Symposium, pp. 153–163 (2021). https://doi.org/10.1007/978-3-030-79561-0_15 . Springer
30. Bauknecht, A., Beyer, Y., Schultz, J., Asaro, S., Khalil, K., Römer, U., Steen, M., Cavaliere, D., Fezans, N.: Novel concepts for active load alleviation. In: AIAA Scitech 2022 Forum. AIAA Paper 2021-1831 (2021). https://doi.org/10.2514/6.2022-0009
31. Harper, C.W., Maki, R.L.: A review of the stall characteristics of swept wings. NASA Technical Note (1964)
32. Diekmann, J.H.: Flight mechanical challenges of stol aircraft using active high lift. J. Aircr. **56**(5), 1753–1764 (2019). https://doi.org/10.2514/1.C034910
33. Leishman, J.G.: Unsteady lift of a flapped airfoil by indicial concepts. J. Aircr. **31**(2), 288–297 (1994). https://doi.org/10.2514/3.46486
34. Phillips, W.F., Snyder, D.O.: Modern adaptation of Prandtl's classic lifting-line theory. J. Aircr. **37**(4), 662–670 (2000). https://doi.org/10.2514/2.2649
35. Wild, J., Pott-Pollenske, M., Nagel, B.: An integrated design approach for low noise exposing high-lift devices. In: 3rd AIAA Flow Control Conference, AIAA Paper 2006-2843 (2006). https://doi.org/10.2514/6.2006-2843

Publisher's Note Springer Nature remains neutral with regard to jurisdictional claims in published maps and institutional affiliations.